Magnetic anomaly navigation using Particle Filtering and an enhanced velocity propagation model[1]

Dominik Pisarski[2], Błażej Popławski, Łukasz Jankowski, Rami Faraj

Institute of Fundamental Technological Research, Polish Academy of Sciences, Pawińskiego 5B, 02-106 Warsaw, Poland

Abstract

This paper proposes a novel velocity estimation technique and integrates it with the Particle Filter to achieve precise positioning of an object moving within a magnetic anomaly field. To estimate the position in GNSS-denied environments, acceleration measurements acquired from the Inertial Measurement Unit are combined with magnetic field measurements and a magnetic anomaly map. The magnetic field measurements are utilized at two levels. First, Bayesian inference is applied to process the rate of change of the magnetic field along the object's trajectory in order to refine the velocity acquired from the Inertial Measurement Unit. This refined velocity estimation serves as an input for the propagation model of the Particle Filter, which subsequently uses the magnetic field measurement and the magnetic anomaly map to estimate the object's position. The proposed method was tested for navigating an unmanned aerial vehicle (UAV) using the ArduPilot simulator across a variety of realistic scenarios. The results demonstrate the efficacy of Bayesian-based velocity estimation in enhancing the classical Particle Filter approach, leading to a substantial reduction in the mean trajectory error. The developed method improves GNSS-independent positioning and navigation and holds promise for applications in various aircraft and robotic systems.

Keywords: Magnetic anomaly navigation, Particle Filter, Bayesian inference, unmanned aerial vehicle, sensor fusion

1. Introduction

The role of Global Navigation Satellite Systems (GNSS) in precise navigation systems is indisputable. However, the GNSS signals can often be degraded or obstructed not only indoors but also in outdoor environments, such as dense urban areas, tunnels, narrow valleys, and even on flat open areas under critical ionosphere and troposphere conditions [1]. Further threats to GNSS-based navigation systems are related to intentional disruptions. Since GNSS signals operate at relatively low power, they are vulnerable to jamming. In the context of Unmanned Aerial Vehicles (UAVs), another significant risk is GNSS spoofing [2]. Researchers and engineers are therefore continually driven to explore alternatives to Global Navigation Satellite Systems (GNSS) that could provide safe and precise positioning.

A broad class of modern navigation systems developed for operating in GNSS-denied environments relies on vision-based technologies that employ terrain and infrastructure features for position referencing. Comprising high spatial resolution and relatively low-cost instrumentation, vision-based systems have found numerous applications in UAV technology, serving as an alternative or a complement to Inertial Navigation Systems (INS) [3, 5, 6]. However, the vision-based systems face several limitations including high computational

[1]Preprint of the manuscript submitted to "Measurement" on March 21, 2025. The final published version is available at https://doi.org/10.1016/j.measurement.2026.121656 (Measurement 278:121656, 2026).

[2]Correspondence to: dpisar@ippt.pan.pl

requirements, suitability primarily for close-ground travel, reliance on adequate lighting conditions, and vulnerability to rapid motion or adverse environmental conditions such as fog, rain, snow, or dust [7]. Additionally, their dependence on terrain diversity makes vision-based systems unsuitable for use in flat deserts, vast forests, or open water. Another GNSS-independent approach for navigation employs gravity gradiometers that return information on the gravity gradient tensor [8]. The gradiometers were originally intended to replace sonars in submarine operations, not only for navigation, but also for collision avoidance [9] and the detection of underground resources [10]. Numerous advancements in gradiometer-based systems have also been introduced in aviation [11, 12], including the application for positioning over open waters [13]. The main challenge of the gradiometer-based systems lies in distinguishing between the effects related to gravity and inertial forces. The problem is particularly evident in the case of smaller UAVs, which permanently experience rapid changes in orientation. Additionally, the need to minimize overall weight does not allow for the installation of equipment necessary to mitigate the influence of the inertial effects, such as stabilizers or high-precision inertial measurement units.

In parallel to vision-based systems and gradiometry, recent advancements in positioning and navigation systems have drawn special attention to the use of crustal magnetic anomalies. Magnetic signals can be measured in both indoor and outdoor environments without constraints on daily time frames. Due to the significant variability in the distribution of magnetic anomalies across most terrains, they provide a reliable reference for positioning, also in the environments that may appear uniform to camera-based systems. Thanks to the lightweight design of magnetometers, magnetic anomaly-based navigation systems can be implemented on ultralight UAV platforms. Moreover, efficient calibration procedures [14, 15] ensure that magnetic field measurements remain consistent despite the dynamic characteristics of flight.

Various methodologies have been developed to date for positioning and navigation based on the magnetic field, designed to meet the specific characteristics of the environment. For indoor applications, a widely used approach is Simultaneous Localization and Mapping (SLAM), which was developed for robotic platforms and involves both mapping the ambient magnetic field and localizing within the environment [16–18]. To determine the actual location, SLAM typically combines data from a magnetometer with onboard motion sensors and employs Kalman filters [19] or particle filters [20, 21] for processing. In [22], an extended Kalman filter was used to fuse data from a magnetometer and an Inertial Measurement Unit (IMU) to estimate the position of a model ship. In [23], a gradient-based Kalman filter and a dynamic system were developed to reduce noise in magnetic field measurements, enhancing IMU performance in position estimation for a foot-mounted application. A sequential batch fusion algorithm for indoor magnetic map matching, employing magnetometers, gyroscopes, and wheel odometry, was proposed in [24]. A computationally efficient algorithm based on Bayesian inference, which fuses data from an IMU and a magnetometer, was proposed in [29]. In addition to indoor applications, outdoor implementations have also been reported. In particular, airborne magnetic anomaly navigation was successfully used to determine the absolute position of aircraft [25, 26]. Similar to indoor systems, these solutions employ map-matching techniques that use scalar magnetic measurements to reduce drift in the inertial navigation system. During flight demonstrations, including over hour-long flights, the accuracy achieved was within tens of meters [27]. Recent literature also highlights the use of machine learning, which has been shown to be effective for in-flight magnetic navigation [28].

The present paper focuses on magnetic field–based navigation for aerial systems using the Particle Filter. Compared to the previous works, it contributes to the development of the propagation model (also referred to as the motion model), which is embedded in the structure of the Particle Filter [30, 31] as a module responsible for kinematics. Typically, the propagation model estimates velocity by integrating data from motion sensors, which poses challenges in airborne applications due to inherent IMU drift. This work proposes fusing information from IMU and magnetometer at the level of velocity estimation, to ensure reliable outputs from the propagation model, ultimately enhancing the positioning accuracy achieved by the Particle Filter. This approach leads to dual use of magnetic field measurements. First, the rate of change of the magnetic

field along the object's trajectory is fed into the propagation model to estimate the particles' velocity. Then, the absolute magnetic field values are compared with a magnetic anomaly map to update the particles' weights and refine the position estimate. Since the proposed method affects the embedded structure of the Particle Filter algorithm, validation is divided into two distinct parts. The first part examines the velocity estimation performance and its impact on Particle Filter outputs. This is conducted in an open-loop setting, where the UAV dynamics are neglected, and the positioning accuracy of the Particle Filter algorithm is analyzed under assumed IMU drift. Thereafter, closed-loop simulations employing ArduPilot are performed in the second part to validate the method within the xt of the coupling between the Particle Filter and UAV dynamics. In addition, the method is tested for robustness under a range of uncertainties present in flight scenarios.

The remaining part of this paper is structured as follows. Section 2 discusses the composition of the magnetic field–based navigation system, outlining the underlying assumptions and objectives. Next, the enhanced velocity propagation model is developed and integrated into the Particle Filter algorithm. Section 3 presents the results of the open-loop simulations that validate the performance of the proposed magnetic correction to velocity estimation. Section 4 demonstrates the effectiveness of the developed method in the context of its integration with a UAV navigation system. Finally, Section 5 summarizes the findings and provides the concluding remarks.

List of symbols

2. Particle Filter with enhanced velocity propagation model

2.1. Problem statement

Consider the problem of estimating the position of a navigating UAV without relying on absolute position information from GNSS. In such scenarios, the IMU becomes the primary data source for localization. Unlike encoders used in ground-based systems, which provide reliable movement data for ground platforms, inertial modules are prone to drift due to the integration of accelerations measured with finite precision. To ensure high-accuracy positioning, we propose using a Particle Filter that incorporates magnetometer readings at two distinct stages, as illustrated in Fig. 1. In the first stage, data from the magnetometer, IMU, and a magnetic anomaly map is fused and used for velocity estimation, which then serves as the input to the Particle Filter (PF). In the second stage, the PF integrates the magnetic field measurements, the magnetic anomaly map, and the estimated velocity within its propagation model. This design can serve as a viable alternative to a GNSS-based positioning module, which is typically a key input to the Kalman Filter integrated in UAV autopilot systems.

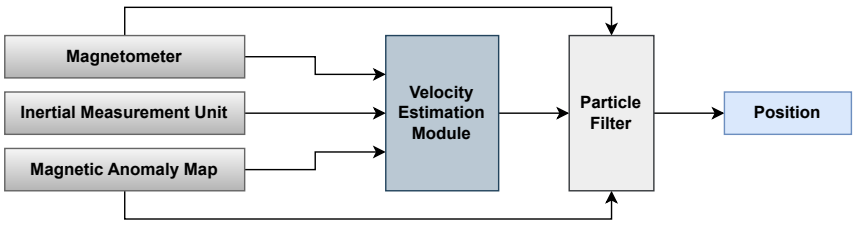

Figure 1: Scheme of the proposed positioning system. Magnetometer data is used at two levels: to refine the velocity output from the IMU and to estimate the position through the Particle Filter.

The proposed positioning system aims to estimate the object's position while reducing the uncertainty of the estimation. To achieve this, the paper focuses on two specific objectives:

Table 1: List of symbols

$\mathbf{w} \in \mathbb{R}^2$	velocity (deterministic two-element vector)
$f_{\mathbf{A}}(\mathbf{w})$	probability density function of the random variable $\mathbf{A}$
$\boldsymbol{\mu}_{\mathbf{A}}$	expected value of the random variable $\mathbf{A}$
t	time step
$\mathbf{V}_t$	velocity determined at time step t by the proposed system (2D random variable)
$\mathbf{V}_t^{\mathrm{IMU}}$	IMU-based velocity at time step t (2D random variable)
$\Delta\mathbf{V}_t^{\mathrm{IMU}} = \mathbf{V}_t^{\mathrm{IMU}} - \mathbf{V}_{t-1}^{\mathrm{IMU}}$	IMU-based velocity increment at time step t (2D random variable)
$\bar{\mathbf{V}}_t = \mathbf{V}_{t-1} + \Delta\mathbf{V}_t^{\mathrm{IMU}}$	velocity at time step t obtained by updating $\mathbf{V}_{t-1}$ by $\Delta\mathbf{V}_t^{\mathrm{IMU}}$ (2D random variable)
$\mathbf{W}_t = \bar{\mathbf{V}}_t\|_{\bar{\mathbf{V}}_t = \mathbf{V}_t^{\mathrm{IMU}}}$	velocity obtained by fusing $\bar{\mathbf{V}}_t$ and $\mathbf{V}_t^{\mathrm{IMU}}$ (2D random variable)
$\mathbf{x}_t, \bar{\mathbf{x}}_t \in \mathbb{R}^2$	locations in a 2D space at time step t (deterministic two-element vectors)
$M(\mathbf{x})$	magnetic field at location $\mathbf{x}$
$\nabla M(\mathbf{x})$	gradient of the magnetic field at location $\mathbf{x}$ (deterministic two-element vector)
$G_t \sim \mathcal{N}(\mu_{G_t}, \sigma_{\mathrm{G}}^2)$	time derivative of the measured magnetic field (1D random variable), as estimated at time step t from the in-flight magnetic field measurements
$\delta(\cdot)$	Dirac delta function defining the probability distribution generated by the Particle Filter
n_t	number of particles at time step t
Δt	time step
ϕ	latitude
λ	longitude
σ_{M}	magnetic field measurement noise
σ, l	hyperparameters of the Gaussian regression
ϵ	error of the initial position
E	average position error
err_i	position error relative to waypoint i
MAE	mean absolute error
KPD	kilometers per degree

G1. Precise estimation of the object's velocity by using Bayesian inference for data fusion of inertial measurements and magnetic field readings.
G2. Computation of the object's position within the Particle Filter by using magnetic field values, the magnetic anomaly map, and the enhanced velocity input.

To ensure the operation of the proposed positioning system, the following assumptions must be satisfied:

A1. The drift in the UAV velocity estimated from the IMU is sufficiently small.
A2. The magnetic anomaly field within the object's movement area is stationary over time.
A3. Magnetic anomalies are mapped with sufficient accuracy.
A4. The magnetic anomaly field has continuous spatial derivatives.
A5. The quality of the magnetometer measurements is sufficient to obtain a smooth time derivative of the magnetic anomaly field.

Specifically, A1 ensures that the velocity provided by the IMU, even if imprecise, remains suitable for processing in the velocity estimation module, where it is fused with magnetometer data. A2–A4 ensure the relevance of the predefined magnetic anomaly map for reference positioning. Finally, A5 is necessary for performing Bayesian inference during the magnetic field–based velocity estimation (see Section 2.3).

2.2. Generalized Particle Filter algorithm

The Particle Filter aims to sequentially estimate the distribution p of the state X_t at time t given the observation z_t:

$$p(X_t|z_t) = \sum_{i=1}^{n_t} w_t^i \, \delta(X_t - \mathbf{x}_t^i), \tag{1}$$

In Eq. (1), δ represents the Dirac delta function, n_t stands for the number of particles, and $\mathbf{x}_t^1, ..., \mathbf{x}_t^{n_t}$ and $w_t^1, ..., w_t^{n_t}$ denote the particles locations and their weights, respectively. In the standard version of the Particle Filter ([30]), the computation of the distribution in Eq. (1) relies on the three major steps:

Step A. Calculation of the weights w_t^i, $i = 1, ..., n_t$, which are proportional to the measurement density $p(z_t|X_t)$.

Step B. Re-sampling, which involves discarding the least significant particles and generating new particles according to $p(z_t|X_t)$, resulting in a new set of particles with a total number n_{t+1} to be considered at the next time step $t + 1$.

Step C. The positions of particles at time $t+1$ are updated by employing a propagation model, i.e., $\mathbf{x}_{t+1}^i = P(\mathbf{x}_t^i)$, $i = 1, ..., n_{t+1}$, where P represents the assumed propagation model.

In the considered setup, the propagation model P depends on the estimated velocity, which, in UAV applications, is typically derived by integrating the acceleration data from the IMU. However, since the velocity estimated from the IMU alone is susceptible to significant drift, this paper incorporates a magnetic field correction into the velocity estimation process to improve the performance of the propagation model.

2.3. The propagation model: velocity correction via magnetic field measurement and Bayesian inference

This section proposes a Bayesian data fusion procedure that corrects the IMU-based velocity using in-flight magnetometric measurements. The procedure is used in each time step t after calculating the IMU-based velocity $\mathbf{V}_{t+1}^{\text{IMU}}$ but before feeding the velocity to the Particle Filter (see Fig. 1). The input data in each step consists of, see Table 1:

- The data available at time step t, that is: the deterministic locations of particles $\mathbf{x}_t^i$, $i = 1, ..., n_{t+1}$, after re-sampling (see Step B), and their probabilistically modeled velocity $\mathbf{V}_t$.
- New data gathered during the next time step $t + 1$, that is: the IMU-based velocity $\mathbf{V}_{t+1}^{\text{IMU}}$ and its update $\Delta\mathbf{V}_{t+1}^{\text{IMU}}$, and the time derivative g_{t+1} of the magnetic field estimated using the current in-flight magnetometric measurements (specific realization of the random variable G_{t+1}).

The output in each step consists of the updated deterministic locations of the particles $\mathbf{x}_{t+1}^i$, $i = 1, ...n_{t+1}$, and their probabilistically modeled velocity $\mathbf{V}_{t+1}$. The proposed propagation model P updates the particle locations using a procedure similar to Euler's scheme of numerical integration. This scheme is first-order, and its simplicity allows the location update to be separated from the velocity update. The procedure is realized through three steps:

Step 1. *Particle location update.* The particle locations are updated using the expected value of the velocity $\mathbf{V}_t$, denoted as $\boldsymbol{\mu}_{\mathbf{V}_t}$:

$$\mathbf{x}_{t+1}^i = \mathbf{x}_t^i + \Delta t \, \boldsymbol{\mu}_{\mathbf{V}_t}, \;\; i = 1, ..., n_{t+1}. \tag{2}$$

Step 2. *Processing of the IMU-based velocity.* First, the velocity information from the previous step is updated using the IMU-based velocity increment, $\bar{\mathbf{V}}_{t+1} = \mathbf{V}_t + \Delta\mathbf{V}_{t+1}^{\text{IMU}}$. Assuming for simplicity that the

summands are independent:

$$\boldsymbol{\Sigma}_{\bar{\mathbf{V}}_{t+1}} = \boldsymbol{\Sigma}_{\mathbf{V}_t} + \boldsymbol{\Sigma}_{\Delta\mathbf{V}_{t+1}^{\mathrm{IMU}}}, \tag{3a}$$

$$\boldsymbol{\mu}_{\bar{\mathbf{V}}_{t+1}} = \boldsymbol{\mu}_{\mathbf{V}_t} + \boldsymbol{\mu}_{\Delta\mathbf{V}_{t+1}^{\mathrm{IMU}}}. \tag{3b}$$

Then, the velocity information provided by the random variables $\bar{\mathbf{V}}_{t+1}$ and $\mathbf{V}_{t+1}^{\mathrm{IMU}}$ is fused into a single random variable $\mathbf{W}_{t+1}$. The Bayesian formalism is used for this purpose, where the natural condition $\bar{\mathbf{V}}_{t+1} = \mathbf{V}_{t+1}^{\mathrm{IMU}}$ plays the role of the evidence. Under the simplifying assumption of independence of $\bar{\mathbf{V}}_{t+1}$ and $\mathbf{V}_{t+1}^{\mathrm{IMU}}$,

$$f_{\mathbf{W}_{t+1}}(\mathbf{w}) = f_{\bar{\mathbf{V}}_{t+1}|\bar{\mathbf{V}}_t=\mathbf{V}_{t+1}^{\mathrm{IMU}}}(\mathbf{w}) \sim f_{\bar{\mathbf{V}}_{\mathbf{t+1}}}(\mathbf{w}) f_{\mathbf{V}_{t+1}^{\mathrm{IMU}}}(\mathbf{w})$$

and thus $\mathbf{W}_{t+1}$ has a Gaussian distribution

$$\mathbf{W}_{t+1} \sim \mathcal{N}\left(\boldsymbol{\mu}_{\mathbf{W}_{t+1}}, \boldsymbol{\Sigma}_{\mathbf{W}_{t+1}}\right)$$

with the following mean and covariance matrix:

$$\boldsymbol{\Sigma}_{\mathbf{W}_{t+1}} = \left(\boldsymbol{\Sigma}_{\bar{\mathbf{V}}_{t+1}}^{-1} + \boldsymbol{\Sigma}_{\mathbf{V}_{t+1}^{\mathrm{IMU}}}^{-1}\right)^{-1}, \tag{4a}$$

$$\boldsymbol{\mu}_{\mathbf{W}_{t+1}} = \boldsymbol{\Sigma}_{\mathbf{W}_{t+1}} \left(\boldsymbol{\Sigma}_{\bar{\mathbf{V}}_{t+1}}^{-1} \boldsymbol{\mu}_{\bar{\mathbf{V}}_{t+1}} + \boldsymbol{\Sigma}_{\mathbf{V}_{t+1}^{\mathrm{IMU}}}^{-1} \boldsymbol{\mu}_{\mathbf{V}_{t+1}^{\mathrm{IMU}}}\right). \tag{4b}$$

Step 3. *Processing of the magnetometric measurements.* The information provided by $\mathbf{W}_{t+1}$ is fused with the information provided by the time derivative g_{t+1} of the magnetic field into the final velocity $\mathbf{V}_{t+1}$. The time derivative of the magnetic field is estimated during flight from measurements, and $G_{t+1} = g_{t+1}$ is treated as the available evidence. Let the updated location be $\mathbf{x}_{t+1}$. Using the Bayesian formalism and assuming the independence of $\mathbf{W}_{t+1}$ and G_{t+1},

$$f_{\mathbf{V}_{t+1}}(\mathbf{w}) = f_{\mathbf{W}_{t+1}|G_{t+1}=g_{t+1}}(\mathbf{w}) \sim f_{\mathbf{W_{t+1}},G_{t+1}}(\mathbf{w}, g_{t+1}) = f_{\mathbf{W_{t+1}}}(\mathbf{w}) f_{G_{t+1}}(g_{t+1}).$$

The final velocity $\mathbf{V}_{t+1}$ is thus normally distributed:

$$\mathbf{V}_{t+1} \sim \mathcal{N}\left(\boldsymbol{\mu}_{\mathbf{V}_{t+1}}, \boldsymbol{\Sigma}_{\mathbf{V}_{t+1}}\right),$$

where

$$\boldsymbol{\Sigma}_{\mathbf{V}_{t+1}} = \left(\boldsymbol{\Sigma}_{\mathbf{W}_{t+1}}^{-1} + \frac{\nabla M(\mathbf{x}_{t+1}) \left(\nabla M(\mathbf{x}_{t+1})\right)^{\mathrm{T}}}{\sigma_{\mathrm{G}}^2}\right)^{-1}, \tag{5a}$$

$$\boldsymbol{\mu}_{\mathbf{V}_{t+1}} = \boldsymbol{\mu}_{\mathbf{W}_{t+1}} + \frac{g_{t+1} - \boldsymbol{\mu}_{\mathbf{W}_{t+1}}^{\mathrm{T}} \nabla M(\mathbf{x}_{t+1})}{\sigma_{\mathrm{G}}^2} \boldsymbol{\Sigma}_{\mathbf{V}_{t+1}} \nabla M(\mathbf{x}_{t+1}). \tag{5b}$$

The output is the updated location $\mathbf{x}_{t+1}$ (computed by Eq. (2) in Step 1) and the corrected velocity $\mathbf{V}_{t+1}$ (computed by Eq. (5) in Step 3).

3. Performance evaluation

This section examines the effectiveness of the velocity correction proposed in Section 2.3. The tests are conducted using simulations of the positioning provided by the Particle Filter (Steps A–C), where the velocity in the propagation model (Step C) is computed either by integrating the accelerations provided by

the IMU or by using the proposed fusion of measurements from the IMU and magnetometer (Steps 1–3). The simulations are carried out assuming the flight trajectory described in Section 3.2. To implement the velocity correction, a magnetic anomaly map satisfying the regularity assumption A4 must first be introduced (see Section 2.1).

3.1. Magnetic anomaly mapping

To date, several approaches have been proposed to create a reference magnetic anomaly map that guarantees sufficient accuracy for precise positioning and navigation. In [32], the authors proposed using linear interpolation on magnetic measurement data collected in a grid. In [33], the magnetic field was represented using the spatial binning method. In the present paper, we seek a smooth representation of the magnetic anomaly and, therefore, adopt the approach based on Gaussian regression [34, 35]. In addition to providing the required regularity (assumption A4), this technique has also proven effective in reconstructing typical characteristics of the crustal magnetic field with limited measurements [20].

To perform Gaussian regression on the magnetic anomaly field, the first step is to acquire a set of m measurements $M^1(\bar{\mathbf{x}}^1), ..., M^m(\bar{\mathbf{x}}^m)$ at the respective locations $\bar{\mathbf{x}}^1, ..., \bar{\mathbf{x}}^m \in X \subset \mathbb{R}^2$. All measurements are assumed to be distorted with some Gaussian noise $\epsilon \sim \mathcal{N}(0, \sigma_{\mathrm{M}}^2)$. Using the assumption that $M^1(\bar{\mathbf{x}}^1), ..., M^m(\bar{\mathbf{x}}^m)$ represent a Gaussian process $\mathcal{M}$, the function $M : X \to \mathbb{R}$ can be computed as the mean of the posterior distribution, $M(\mathbf{x}) = \mathbb{E}\left[\mathcal{M}(\mathbf{x}) | M^1(\bar{\mathbf{x}}^1), ..., M^m(\bar{\mathbf{x}}^m)\right]$. By applying the Bayes rule [36], the posterior distribution can be expressed as:

$$\mathcal{M}(\mathbf{x}) | M^1(\bar{\mathbf{x}}^1), ..., M^m(\bar{\mathbf{x}}^m) \ \sim \ \mathcal{N}\left(\mu_{\mathcal{M}}, \sigma_{\mathcal{M}}^2\right). \tag{6}$$

In Eq. (6), the mean $\mu_{\mathcal{M}}$ is a function of $\mathbf{x} \in X \subset \mathbb{R}^2$ defined as:

$$\mu_{\mathcal{M}}(\mathbf{x}) = \left[\kappa(\mathbf{x}, \bar{\mathbf{x}}^1), ..., \kappa(\mathbf{x}, \bar{\mathbf{x}}^m)\right]^{\mathrm{T}} \left(\mathbf{C} + \sigma_{\mathrm{M}}\mathbf{I}\right)^{-1} \left[M^1(\bar{\mathbf{x}}^1), ..., M^m(\bar{\mathbf{x}}^m)\right], \tag{7}$$

where κ denotes the covariance kernel function, which is commonly assumed to be represented by a Gaussian function with the signal variance σ^2 and the length scale l:

$$\kappa(\mathbf{x}, \bar{\mathbf{x}}^i) = \sigma^2 \exp\left(-\frac{\|\mathbf{x} - \bar{\mathbf{x}}^i\|^2}{2l^2}\right), \qquad i = 1, ..., m, \tag{8}$$

In Eq. (7), $\mathbf{I}$ stands for the identity matrix and the covariance matrix $\mathbf{C}$ is determined as:

$$\mathbf{C} = \left[c_{i,j}\right]_{m \times m}, \qquad c_{i,j} = \kappa(\bar{\mathbf{x}}^i, \bar{\mathbf{x}}^j). \tag{9}$$

Thus, for each location $\mathbf{x} \in X \subset \mathbb{R}^2$, the function M can be expressed as follows:

$$M(\mathbf{x}) = \mu_{\mathcal{M}}(\mathbf{x}) = \left[\kappa(\mathbf{x}, \bar{\mathbf{x}}^1), ..., \kappa(\mathbf{x}, \bar{\mathbf{x}}^m)\right]^{\mathrm{T}} \left(\mathbf{C} + \sigma_{\mathrm{M}}\mathbf{I}\right)^{-1} \left[M^1(\bar{\mathbf{x}}^1), ..., M^m(\bar{\mathbf{x}}^m)\right]. \tag{10}$$

For the selection of the hyperparameters σ and l in Eq. (8), we perform the maximization of the log marginal likelihood ([37]):

$$\begin{aligned} J(\sigma, l) = &-\frac{1}{2}\left[M^1(\bar{\mathbf{x}}^1), ..., M^m(\bar{\mathbf{x}}^m)\right]^{\mathrm{T}} \left(C + \sigma_{\mathrm{M}} I\right)^{-1} \left[M^1(\bar{\mathbf{x}}^1), ..., M^m(\bar{\mathbf{x}}^m)\right] \\ &-\frac{1}{2}\log\left(\det\left(\mathbf{C} + \sigma_{\mathrm{M}}\mathbf{I}\right)\right) - \frac{m}{2}\log(2\pi). \end{aligned} \tag{11}$$

The determined optimal hyperparameters σ^* and l^* must satisfy the necessary optimality conditions:

$$\frac{\partial J}{\partial \sigma}(\sigma^*, l^*) = 0, \qquad \frac{\partial J}{\partial l}(\sigma^*, l^*) = 0, \tag{12}$$

and they can be computed using the gradient ascent method.

Throughout this work we use for tests a virtual magnetic field map characterized by:

$$\begin{aligned} \mathrm{Map}(\lambda, \phi) =& 51000 + 100\left(0.1 + 5(1-\bar{\lambda})^2 \exp(-\bar{\lambda}^2 - (\bar{\phi}+1)^2) - 2(\bar{\lambda}/15 - \bar{\lambda}^3 - \bar{\phi}^5)\exp(-\bar{\lambda}^2 - \bar{\phi}^2)\right) \\ &+ 100\left(-2\exp(-(\bar{\lambda}+1)^2 - \bar{\phi}^2)\right)\ [\mathrm{nT}], \quad \bar{\lambda} = 20(\lambda - 20.880), \quad \bar{\phi} = 32(\phi - 52.250). \end{aligned} \tag{13}$$

The map's longitude λ and latitude ϕ extend within 20.880–20.935 and 52.250–52.285 degrees, respectively. The assumed magnetic field characteristics represent the combination of the core field and a medium-gradient lithospheric field, typical of the terrain at the respective coordinates [39]. Based on the assumed magnetic field map, $m = 2000$ coordinates $\bar{\mathbf{x}}^1, ..., \bar{\mathbf{x}}^m$ are randomly selected within the specified ranges to generate the set of measurements, $M^1(\bar{\mathbf{x}}^1), ..., M^m(\bar{\mathbf{x}}^m)$, using Eq. (13). Gaussian noise with the standard deviation $\sigma_{\mathrm{M}} = 0.5$ [nT] was added to simulate the performance of modern compact scalar magnetometers [40]. The final magnetic anomaly map, used in the subsequent sections (see Fig. 2 and 5), was obtained through Gaussian regression—Eqs. (8) and (10)—with the hyperparameters $\sigma = 0.004$ and $l = 0.011$ optimized using Eq. (12).

3.2. Flight scenario

The simulations were performed using a flight trajectory (referred to as the *reference trajectory*) generated by the ArduPilot simulator (for more details see Section 4) and defined by nine waypoints (WP-0 to WP-8). These waypoints covered a rectangular area with longitude coordinates approximately ranging from 20.89° to 20.93° and latitude coordinates from 52.26° to 52.28°, as illustrated in Fig. 2. The aircraft performs a vertical takeoff at WP-0, then transitions to airplane mode and sequentially navigates through waypoints WP-1, WP-2, ..., WP-8. Finally, it returns to WP-0, switches back to multi-rotor mode, and lands vertically. The total flight length is approximately 7340 [m]. The averaged flight velocity is 18.91 [m/s]. The considered area encompasses an old military airfield, and the flight itself can be viewed as a patrol operation.

This section examines how the proposed velocity correction enhances IMU readings and impacts the performance of the Particle Filter–based positioning. For this analysis, the focus is on open-loop simulations,

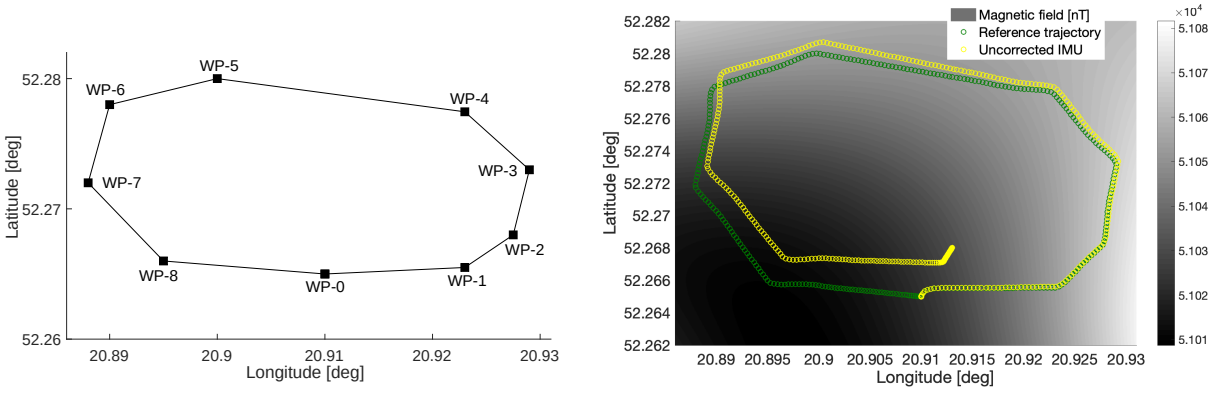

Figure 2: Flight scenario defined by the specified waypoints: takeoff at WP-0, transitions through WP-1, WP-2, ..., WP-8, and landing at WP-0 (left). Flight trajectory generated by the ArduPilot simulator and the corresponding assumed IMU readings, with the magnetic field map displayed in the background (right).

where the positioning generated by the proposed method does not influence the operation of ArduPilot. The reference trajectory was generated under the assumption of full access to GNSS data. All comparisons in this section are based on the same reference trajectory. Closed-loop simulations, which account for the influence of the designed positioning on the ArduPilot controller and the resulting flight trajectories, are discussed in Section 4.

The performance of the velocity correction algorithm developed in Section 2.3 is analyzed in terms of Particle Filter positioning accuracy, considering scenarios with two interrupting factors: IMU drift and initial position error. IMU drift results from the integration of inaccurate acceleration measurements, while the initial position error may arise from disturbances in satellite navigation readings, which were spoofed before the mission began. IMU readings are assumed to exhibit a deterministic velocity drift that increases linearly with time, resulting in a position error of 400 meters by the end of the mission (see the *uncorrected IMU* trajectory in Fig. 2). For the initial position error ϵ, cases within the range of 0 to 200 meters are considered.

3.3. Implementation of the Particle Filter with the enhanced velocity algorithm

The implementation of the general Particle Filter scheme (see Steps A–C in Section 2.2) was carried out under the following assumptions. The state X_t represents the positioning coordinates (longitude and latitude in degrees) at time step t, where $t = 1, ..., T$. Here $t = 1$ and $t = T$ denote the initial and final time steps, respectively. For the considered flight trajectory, which had a total duration of 388 seconds, positioning updates were assumed to occur every second, resulting in $T = 389$. To estimate the initial position at $t = 1$, $n_1 = 100$ particles were assumed, distributed according to a normal distribution centered around the estimated starting position, with a standard deviation of 0.0005 [deg].

At each time step t, the calculation of the weights (Step A) was performed using a Gaussian function p, where the argument was determined by the difference between the measured magnetic reading z_t and the corresponding value from the map. During the re-sampling process (Step B), particles with normalized weights below 0.9 were discarded. New particles were generated by sampling from a normal distribution centered on the remaining particles, with a standard deviation of 0.0002 [deg]. Moreover, the total number of particles was kept within the bounds of 50 to 200.

To update the position of the particles (Step C), the propagation model from Steps 1–3 of the algorithm presented in Section 2.3 was used with the following settings. For Eq. (2), the time step was assumed to be $\Delta t = 1$ [s]. The initial velocity at time step $t = 1$ was set to zero, that is

$$\boldsymbol{\mu}_{\mathbf{V}_1} = \begin{bmatrix} 0 & 0 \end{bmatrix}, \qquad \boldsymbol{\Sigma}_{\mathbf{V}_1} = \begin{bmatrix} 0 & 0 \\ 0 & 0 \end{bmatrix}. \tag{14}$$

The IMU-based velocity increment $\Delta \mathbf{V}_t^{\mathrm{IMU}}$ was assumed to consist of three components: the actual velocity increment of the reference trajectory, a constant factor (drift per second) resulting in the final position error of 400 [m], and a negligibly small random noise. The time derivative of the magnetic field in Eq. (5b) was calculated in Step 3 using the increment of the magnetic readings, expressed as $g_{t+1} = (z_{t+1} - z_t)/\Delta t$. In the simulation, z_t was determined for $t = 1, ..., T - 1$ as the magnetic field readings from the map along the real (reference) trajectory (see Fig. 2), incorporating the assumed measurement noise of 0.5 [nT] (as detailed in Section 3.1). For the variance of the time derivative of the magnetic field measurement (Eq. (5a) and (5b)), we chose $\sigma_{\mathrm{G}}^2 = 0.5$ [nT^2/s^2], which aligns with the assumed magnetic field measurement error.

3.4. Results of open-loop simulations

3.4.1. Analysis of velocity errors

Steps 1–3 of the proposed algorithm (Section 2.3) focus on correcting the velocity. To analyze the effectiveness in velocity correction, 1000 simulations were performed on the reference trajectory, assuming zero initial position error and applying the Particle Filter (Steps A–C) in two different scenarios:

1. *Uncorrected velocity.* The Particle Filter's propagation model (Step C) was fed with the velocity provided by the IMU, including the assumed drift.
2. *Corrected velocity.* The proposed velocity correction was implemented, and the Particle Filter's propagation model processed the already corrected velocity.

The evolution of errors for the uncorrected and corrected velocity, compared to the real velocity along the analyzed trajectory, is illustrated in Fig. 3. The uncorrected IMU velocity exhibits the assumed linear drift, accumulating an error of 2.06 [m/s] (10.9% of the averaged flight velocity) over 389 time steps. The corrected velocity is represented by the mean derived from 1000 simulations (red curve), with the lower and upper bounds (black curves) determined at one standard deviation. In the initial stage of the simulation, for time steps $t \leq 3$, the error of the corrected velocity increases rapidly. This occurs because particles are randomly selected within a relatively large initial radius, which causes temporary fluctuations in the positioning estimates generated by the Particle Filter. For time steps $26 \leq t \leq 65$, the mean error of the corrected velocity remains higher than that of the uncorrected IMU velocity. This is the stage when the Particle Filter works to converge its estimate toward the true position. The maximum of the mean error occurs at $t = 38$, reaching 0.96 [m/s] (5.1% of the average flight velocity). For the remainder of the simulation, the mean error of the corrected velocity remains consistently below 0.8 [m/s]. When averaged over the entire simulation, the error of the corrected velocity is 56.5% lower than that of the uncorrected IMU velocity.

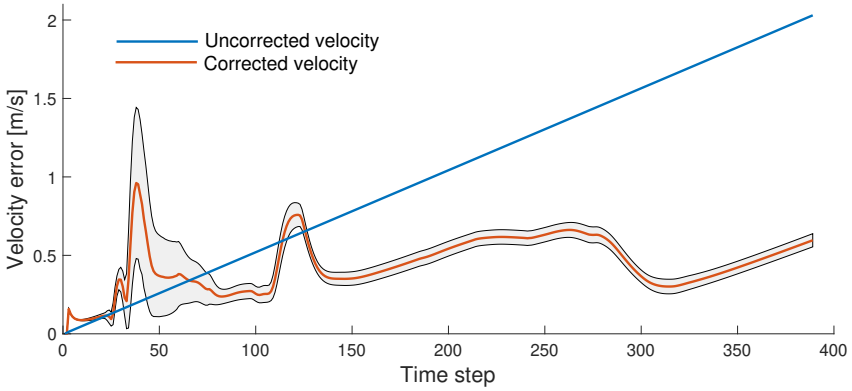

Figure 3: Comparison of uncorrected velocity (IMU-based) and corrected velocity (computed using Steps 1–3 of the developed algorithm). The corrected velocity is represented by the mean of 1000 simulations (red curve), with the lower and upper bounds (black curves) at one standard deviation apart from the mean.

3.4.2. Analysis of positioning errors

To evaluate the positioning accuracy of the proposed method, position errors are analyzed along the assumed flight trajectory using the Particle Filter incorporating both the uncorrected and corrected velocity. With the initial position error set to zero ($\epsilon = 0$), 1000 simulations were conducted for each Particle Filter scenario. The results are illustrated in Fig. 4. By analyzing the mean errors (red curves), a similar performance is observed during the initial stage of the simulation ($t < 30$), and the errors of the uncorrected and corrected velocities are comparable. A clear divergence occurs for $t > 110$, where, in the uncorrected velocity case, the mean position error increases rapidly, reaching 110.4 [m] at time step $t = 213$. In contrast, the proposed velocity correction leads to a significant reduction in the mean position error, and for 92% of the simulation time the mean error remains below 20 [m]. The maximum position error occurs at time step $t = 222$, reaching 23.9 [m], which is 78.3% lower than the peak value in the uncorrected velocity scenario. Overall, the proposed velocity correction reduces the average mean position error E by 78.6% (see Table 2).

Moreover, the overall variation in position error is significantly lower when applying the proposed velocity correction. The trajectories obtained for the considered positioning methods are compared in Fig. 5.

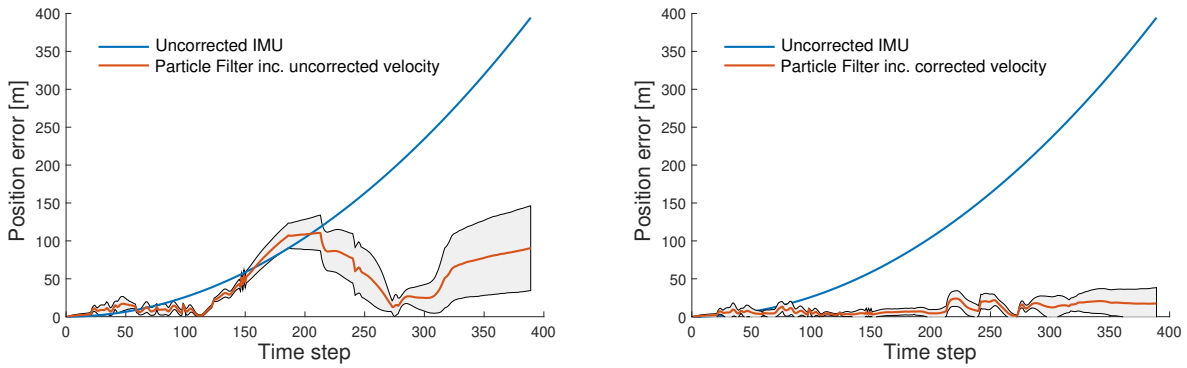

Figure 4: Comparison of positioning accuracy using the Particle Filter incorporating uncorrected velocity (left) and corrected velocity (right) for zero initial error ($\epsilon = 0$). The red curves indicate the mean position errors of 1000 simulations, while the black curves represent the lower and upper bounds, calculated at one standard deviation. The results are compared to the position error as estimated solely by the IMU (blue curve).

Table 2: Average position errors obtained for the two considered positioning methods and different errors of the initial position.

Initial error (ϵ) [m]	Average position error (E) [m]		
	Uncorrected IMU	PF inc. uncorrected vel.	PF inc. corrected vel.
0	132.018	47.126	10.053
50	182.018	50.422	18.363
100	232.018	54.915	22.818
200	332.018	65.056	32.241

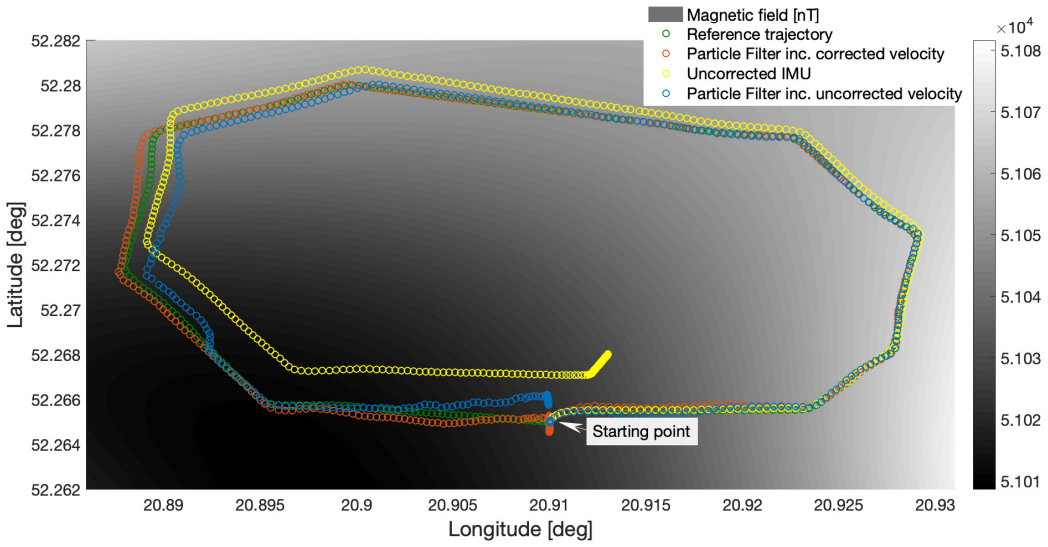

Figure 5: Comparison of the trajectories obtained for the considered positioning methods and zero initial error ($\epsilon = 0$). The assumed magnetic field map is displayed in the background. For the Particle Filter incorporating uncorrected and corrected velocities, the results are based on randomly selected simulations from a set of 1000.

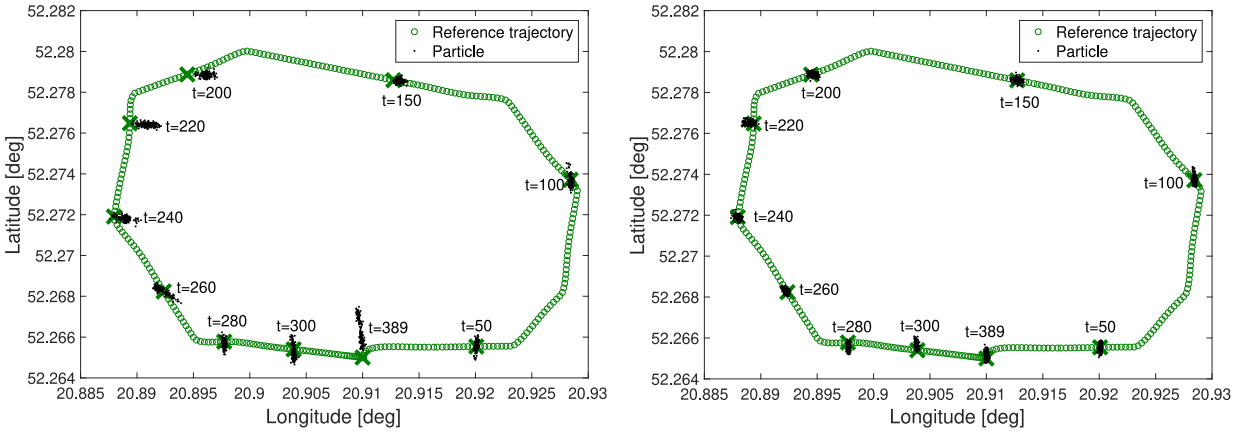

Figure 6: Comparison of particle distributions at selected time steps for uncorrected velocity (left) and corrected velocity (right), with the reference trajectory depicted in the background (green circles with green crosses indicate the reference positions at the analyzed time steps). Results are based on randomly selected simulations from a set of 1000.

To further validate the results, Fig. 6 compares the evolution of particle distributions at selected time steps generated by the Particle Filter for a randomly chosen simulation from a set of 1000. For time steps 50 and 100, the distributions for uncorrected and corrected velocity appear very similar. However, by time step 150, the uncorrected velocity leads to a noticeable backward shift, consistent with the earlier observation in the position error curve (Fig. 4). For time steps 200–260, the uncorrected velocity exhibits a continued backward shift and a gradual deviation from the reference trajectory. In contrast, the corrected velocity maintains a consistently low-error trajectory during the same period. At $t = 280$, the diversity of the particle distributions generated by both configurations is significantly reduced, leading to similar position estimates. However, in the final stage of the flight (time steps 300–389), a gradual divergence in the particle distributions from both configurations becomes evident. Specifically, in the uncorrected case, the particle distribution at $t = 389$ is split into two parts, which results in a significant position estimation error. It is worth noting that the corrected velocity not only ensured more accurate positioning but also produced more consistent particle distributions throughout the entire flight, minimizing abrupt jumps in the Particle Filter's output.

Finally, the simulations were repeated with errors ϵ of the initial position ranging from 50 to 200 [m]. The results for $\epsilon = 50$ [m] are illustrated in Fig. 7. The Particle Filter is capable of rapidly canceling the initial error of 50 [m] in both considered scenarios, and the overall performance of the corrected velocity approach remains consistent with the previous findings. The corrected velocity approach remains superior over the uncorrected case also for the other initial position errors, as summarized in Table 2.

4. UAV navigation system implementation

In the early stages of implementation, newly developed software systems for aircraft are prone to malfunctions. High risk of crashing a real-life test vehicle—whose cost is relatively high even for UAVs—prompts extensive use of simulation tools. Popular UAV autopilot systems can simulate many different aircraft models in various environments thanks to a feature called software-in-the-loop (SITL). Communication with the SITL environment is possible through well-established protocols such as MAVLink [41] or DroneCAN [42], allowing its capabilities to be extended with user-developed scripts. This enables the modeling of Earth's magnetic field distribution, the simulation of magnetometer readings, and the virtual testing of a UAV equipped with position-estimation software based on these data. For this study, ArduPilot's SITL [43] was selected as the simulation environment. The UAV used for experimental testing was of the QuadPlane type, a hybrid aircraft that integrates the capabilities of a fixed-wing plane and a quadcopter.

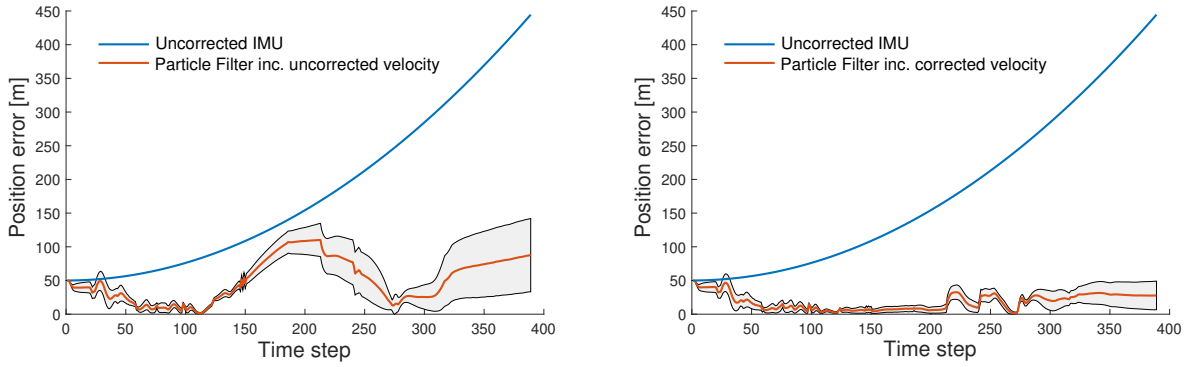

Figure 7: Comparison of positioning accuracy using the Particle Filter incorporating uncorrected velocity (left) and corrected velocity (right) for initial error $\epsilon = 50$ [m]. The red curves indicate the mean position errors of 1000 simulations, while the black curves represent the lower and upper bounds, calculated at one standard deviation. The results are compared to the position error as estimated solely by the IMU (blue curve).

4.1. ArduPilot simulator of UAV platform

Each simulation environment in autopilot software typically consists of at least three fundamental components: the autopilot software, the flight dynamics model, and the Ground Control Station (GCS) software. These components communicate internally using a specific communication protocol, often MAVLink for UAVs. The same protocol can also be used to enable interactions between external scripts and the GCS. The GCS can forward MAVLink messages bidirectionally, both to and from external scripts. This allows users to access data provided to the GCS by the autopilot system, such as telemetry, and to control the software-in-the-loop (SITL) simulation by sending specific MAVLink messages to the GCS. User-developed software interacting with the GCS can further communicate with other software packages via their respective protocols. A common setup involves using Python for communication with the GCS and MATLAB for performing extensive calculations. This combination is also employed in the system described in this paper. Communication between Python and the GCS is handled through the Pymavlink Python module, while interaction between Python and MATLAB scripts is managed via the MATLAB Engine API for Python.

The architecture of the described software-in-the-loop (SITL) environment, enhanced with external user-developed software tailored for the navigation system, is illustrated in Fig. 8. The blue block labeled "*Particle Filter inc. corrected velocity*" represents the MATLAB implementation of the magnetic navigation module, which employs the Particle Filter method incorporating corrected velocity readings. The block labeled "*Python script*" corresponds to the module responsible for facilitating communication between the Ground Control Station (GCS) and MATLAB, as well as handling data processing. The remaining block names are self-explanatory. Additionally, Fig. 9 shows a screenshot of the MAVProxy Ground Control Station (GCS) [44], displaying its Console and Map modules interfacing with ArduPilot's simulation environment.

4.2. Simulation results

A series of simulated flights was conducted based on the scenario outlined in Section 3.2. The effectiveness of the position correction was assessed using a quantitative metric that leverages the predefined waypoints (see Fig. 2). The position error, defined as the minimum distance between the actual trajectory (represented by a series of points j) and a given waypoint i, was computed for each waypoint using the FCC's approximation formula [45]:

$$err_i = \min_j \sqrt{[\mathrm{KPD}_\phi(\phi_i - \phi_j)]^2 + [\mathrm{KPD}_\lambda(\lambda_i - \lambda_j)]^2}. \tag{15}$$

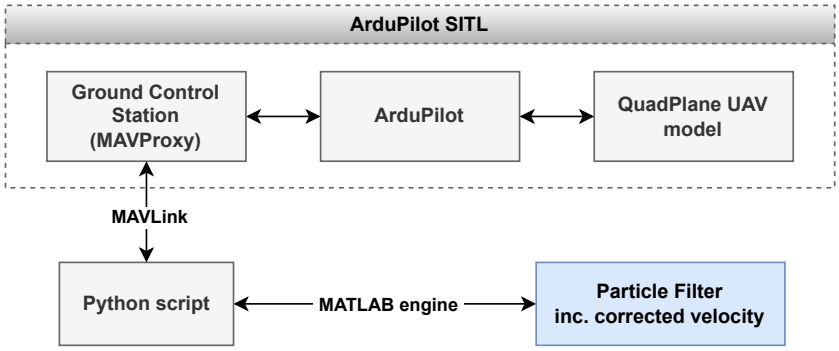

Figure 8: Architecture of the simulation platform.

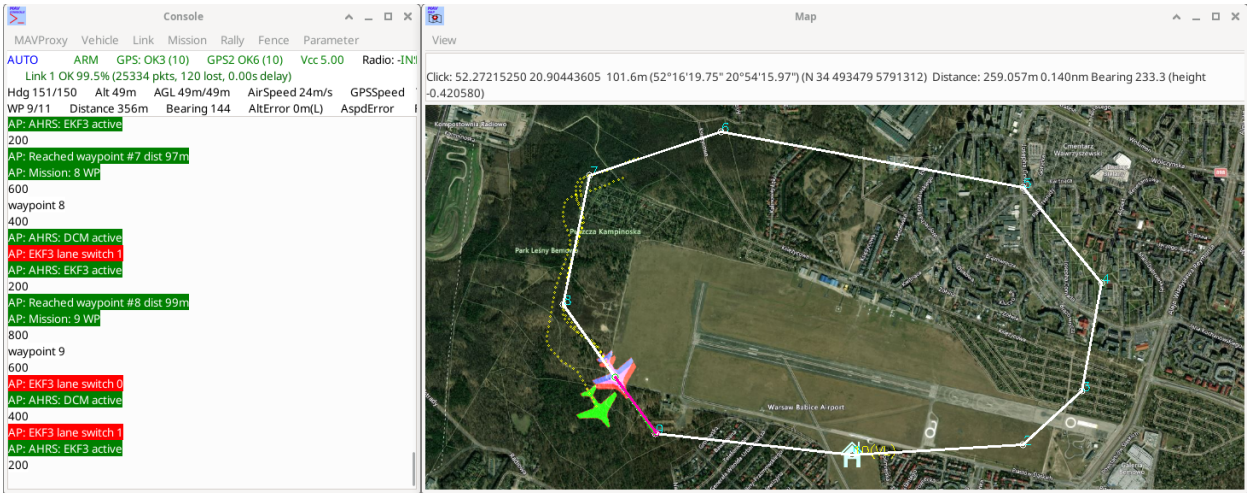

Figure 9: ArduPilot SITL environment: online console (left) and map interface (right).

In Eq. 15, the geographical coordinates ϕ and λ were converted into metric units as follows:

$$\begin{aligned} \mathrm{KPD}_\phi &= 111.13209 - 0.56606\cos(\phi_i + \phi_j) + 0.0012\cos(2(\phi_i + \phi_j)), \\ \mathrm{KPD}_\lambda &= 111.41513\cos(1/2(\phi_i + \phi_j)) - 0.09455\cos(3/2(\phi_i + \phi_j)) + 0.00012\cos(5/2(\phi_i + \phi_j)). \end{aligned} \tag{16}$$

To evaluate the effectiveness of positioning, the average error over 10 realizations of each case was calculated using Eq. (15) for all waypoints in the mission, except WP-0, which is both the starting and landing point.

The flight condition scenarios considered in the simulations were as follows:

- *Case 1* (All sensors operational). All on-board sensors, including the GNSS module, were functioning normally. This case serves as a benchmark for comparison with other scenarios.
- *Case 2* (Uncorrected IMU). The GNSS module either failed or was spoofed. The system relied on the uncorrected IMU velocity, which resulted in a constant drift from the desired trajectory.
- *Case 2* (Particle Filter inc. corrected velocity). The GNSS module either failed or was spoofed. The system relied on the Particle Filter with the proposed magnetic field–based velocity correction.

Figure 10 presents a comparison of the position errors calculated for each waypoint along the trajectory and for all described cases.

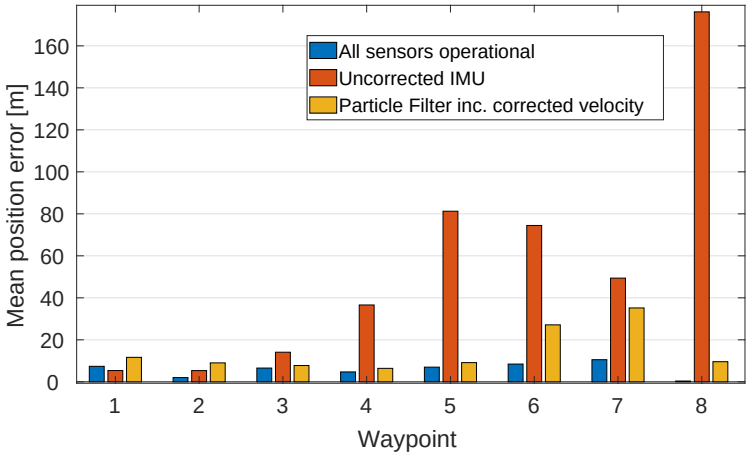

Figure 10: Position errors across all considered flight scenarios.

Case 1 (All sensors operational) exhibits stable, low position errors at each waypoint, as expected when relying on the GNSS system for navigation. In contrast, Case 2 (Uncorrected IMU), where the GNSS module was inoperational and the autopilot relied solely on incremental sensors for position estimation, shows a tendency for the error to increase along the trajectory. Temporary deviations from this trend occur at WP-6 and WP-7 due to nuances in the flight trajectory shape. Case 2 (Particle Filter inc. corrected velocity), which incorporated Particle Filter with the proposed real-time velocity and position corrections derived from magnetic field readings, achieved a significant improvement in positioning accuracy. The mean absolute error (MAE) calculated across all waypoints is 6.55 [m] for Case 1, 47.46 [m] for Case 2 (Uncorrected IMU), and 12.75 [m] for Case 2 (Particle Filter inc. corrected velocity). Selected mission realizations for each described case are illustrated in Fig. 11. The trajectories for Case 1 (All sensors operational) and Case 2 (Particle Filter inc. corrected velocity) closely follow the reference trajectory, demonstrating effective convergence. In contrast, Case 2 (Uncorrected IMU) exhibits significant deviations from the reference trajectory over time.

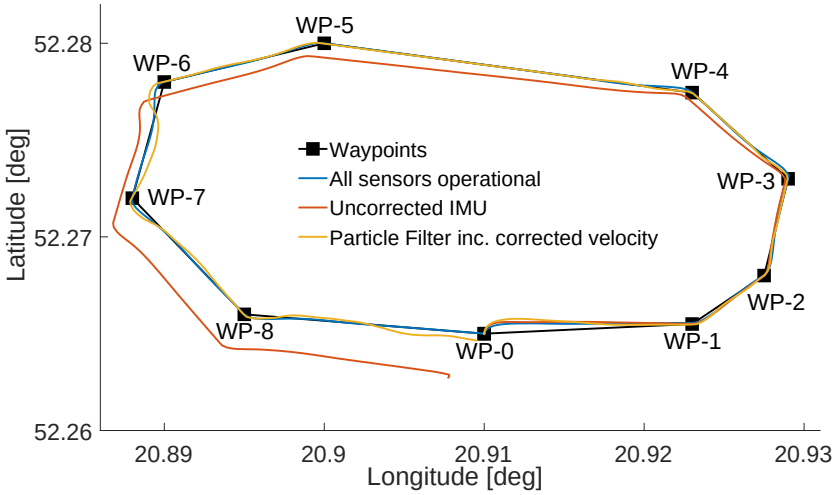

Figure 11: Comparison of exemplary trajectories for the three considered flight scenarios.

4.3. Robustness analysis

An aircraft in flight relies on a variety of systems to estimate its flight parameters. While GNSS module failure is one potential issue, this section evaluates the effectiveness of the proposed positioning method under additional simulated failures of critical flight modules.

A common issue is the malfunction of the pitot tube, a sensor that measures total and static air pressure to estimate airspeed. Incorrect readings can lead to critical flight conditions, such as stalling (caused by overestimated airspeed due to improper calibration) or overspeeding (resulting from underestimated airspeed due to a blocked tube). Such malfunctions can severely impact the aircraft's position estimation, particularly under variable wind conditions. To evaluate the robustness of the proposed alternative navigation system, four additional flight scenarios were examined:

- *Case 3.* Flight with a blocked pitot tube resulting in zero airspeed readings, under no-wind conditions.
- *Case 4.* Flight with a blocked pitot tube and a wind speed of 6 [m/s], typical for the considered geographical region.
- *Case 5.* Flight with an incorrectly calibrated pitot tube causing significantly overstated airspeed readings, under no-wind conditions.
- *Case 6.* Flight with an incorrectly calibrated pitot tube and a wind speed of 6 [m/s].

Each scenario was simulated both with and without Particle Filter correction. Figure 12 presents the position errors for all trajectory waypoints in all these cases, averaged over 10 realizations.

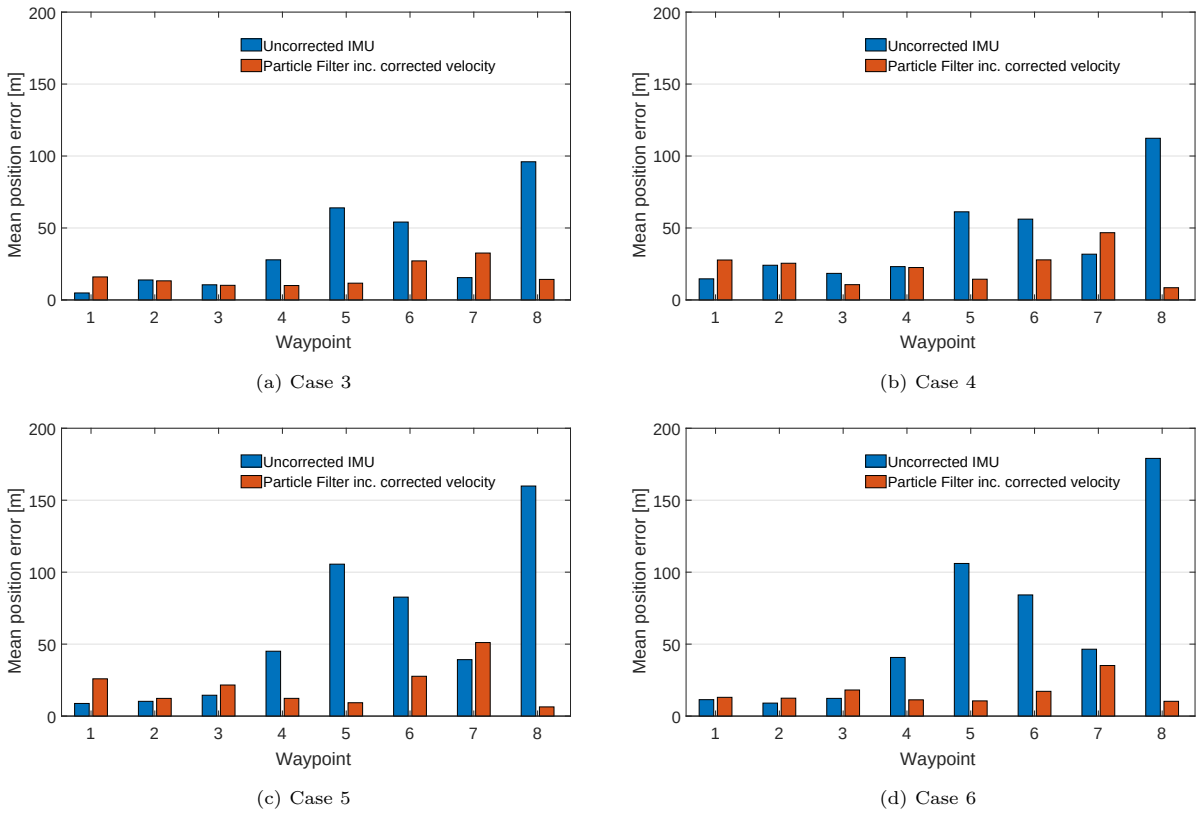

(a) Case 3

(b) Case 4

(c) Case 5

(d) Case 6

Figure 12: Position errors for various pitot tube failures and wind conditions. Case 3: Blocked pitot tube, no-wind conditions; Case 4: Blocked pitot tube, wind speed 6 [m/s]; Case 5: Incorrectly calibrated pitot tube, no-wind conditions; Case 6: Incorrectly calibrated pitot tube, wind speed 6 [m/s].

In general, for the Uncorrected IMU scenarios across all considered cases, improper calibration of the pitot tube results in higher position errors compared to a blocked pitot tube (see Figs. 12a–12d). In each Uncorrected IMU case, the position error tends to increase along the trajectory, except at WP-6 and WP-7, consistent with the observations described in Section 4.2. Integration of the proposed velocity correction method into the UAV navigation system significantly reduces position errors in most cases. However, there are exceptions where applying the magnetic field–based correction results in a slight local decrease in positioning accuracy: WP-1 and WP-7 in Fig. 12a; WP-1, WP-2, and WP-7 in Fig. 12b; WP-1, WP-2, WP-3, and WP-7 in Fig. 12c; WP-1, WP-2, and WP-3 in Fig. 12d. This phenomenon is influenced by several interrelated factors. Key contributors include the distribution of the magnetic field, the resampling rules implemented in the Particle Filter algorithm, the characteristics of the flight trajectory, and environmental conditions. Due to their complex interactions, isolating and quantifying the individual impact of each factor on the observed simulation errors remains challenging.

The proposed method significantly improves positioning accuracy. Table 3 compares the position errors across the considered flight cases, expressed as the mean absolute error calculated for all waypoints in the trajectory. The proposed method reduces the overall position error by at least 46% in Case 4 and up to 74% in Case 6. Compared to Case 1 (All sensors operational), the errors in Cases 2–6 (Uncorrected IMU) are 5.47–9.34 times higher. However, incorporating the Particle Filter with the proposed velocity correction into the navigation system reduces this range to 1.95–3.51 times higher.

Table 3: Mean absolute position error for various pitot tube failures and wind scenarios.

Case No.	MAE [m]		Error reduction [%]
	Uncorrected IMU	PF inc. corrected vel.	
2	47.46 (724)	12.75 (195)	73.13
3	35.84 (547)	16.89 (258)	52.87
4	42.74 (653)	22.99 (351)	46.20
5	58.23 (889)	20.81 (318)	64.26
6	61.15 (934)	16.01 (244)	73.81

Values in parentheses represent percentage position errors relative to Case 1 (All sensors operational), where the position error is 6.55 [m].

5. Concluding remarks

This paper introduced a novel approach for localizing an object operating in a GNSS-denied environment. The method relies on magnetic anomaly measurements, which are internally used within the Particle Filter at its two levels. At the level of velocity estimation, the time derivative of the measured magnetic field is fused with the velocity data acquired from an Inertial Measurement Unit using Bayesian inference. At the level of position estimation, the Particle Filter generates the posterior distribution by utilizing the actual magnetic field value in conjunction with the reference magnetic anomaly map. In open-loop simulations, compared to the Paricle Filter with IMU-based velocity, the proposed enhanced velocity method achieved a significant reduction in the average position error with the improvements ranging from 50.44% to 78.6%. The validation was performed in closed-loop simulations using the ArduPilot simulator and a variety of realistic flight scenarios, including two pitot tube failures and two wind speeds. the Particle Filter with the proposed magnetic field–based correction incorporated into its propagation model was demonstrated to substantially improve the positioning accuracy across all considered scenarios. Compared to the typical use of the IMU based velocity, the reduction of the average position error ranged from 46.20% to 73.81%. The proposed method remained robust with respect to the considered pitot tube failures and wind speeds.

References

[1] N. Crocetto, F. Pingue, S. Ponte, G. Pugliano, V. Sepe, Ionospheric error analysis in GPS measurements, Annals of Geophysics 51 (4) (2008) 585–595. doi:10.4401/ag-4456.

[2] A.J. Kerns, D.P.. Shepard, J.A. Bhatti, A. Jahshan, T.E. Humphreys, Unmanned Aircraft Capture and Control Via GPS Spoofing, Journal of Field Robotics 31 (4) (2014) 617–636. doi:10.1002/rob.21513.

[3] R. Mebarki, V. Lippiello, B. Siciliano, Nonlinear Visual Control of Unmanned Aerial Vehicles in GPS-Denied Environments, IEEE Transactions on Robotics 31 (4) (2015) 1004–1017. doi:10.1109/TRO.2015.2451371.

[4] G. Conte, P. Doherty, Vision-based unmanned aerial vehicle navigation using geo-referenced information, EURASIP Journal on Advances in Signal Processing 2009 (1) (2009) 387308. doi:10.1155/2009/387308.

[5] A. V. R. Katkuri, H. Madan, N. Khatri, A. S. H. Abdul-Qawy, K. S. Patnaik, Autonomous UAV navigation using deep learning-based computer vision frameworks: A systematic literature review, Array, 23 (2024) 100361. doi.org/10.1016/j.array.2024.100361,

[6] Y. Lu, Z. Xue, G. S. Xia, L. Zhang, (2018). A survey on vision-based UAV navigation. Geo-Spatial Information Science, 21(1) (2018), 21–32. doi.org/10.1080/10095020.2017.1420509,

[7] C. Zhu, M. Meurer, C. Günther, Integrity of Visual Navigation—Developments, Challenges, and Prospects, NAVIGATION: Journal of the Institute of Navigation 69(2) (2022). doi.org/10.33012/navi.518,

[8] E. Metzger, Recent gravity gradiometer developments, in: Guidance and Control Conference, American Institute of Aeronautics and Astronautics, Hollywood,FL,U.S.A., 1977, pp. 306–315. doi:10.2514/6.1977-1081.

[9] C. Cevallos, How do submarines use gravity gradients to avoid collisions with underwater mountains?, The Leading Edge, 34(12) 2015, 1426–1544. doi:10.1190/tle34121498.1.

[10] R. E. Bell, Gravity gradiometry, Scientific American 278 (6) (1998) 74–79.

[11] J. Richeson, D. Pines, GPS denied inertial navigation using gravity gradiometry, in: AIAA Guidance, Navigation and Control Conference and Exhibit, American Institute of Aeronautics and Astronautics, Hilton Head, South Carolina, 2007, pp. 1–23. doi:10.2514/6.2007-6791.

[12] T. C. Welker, M. Pachter, R. E. Huffman, Gravity gradiometer integrated inertial navigation, in: 2013 European Control Conference (ECC), IEEE, Zurich, 2013, pp. 846–851. doi:10.23919/ECC.2013.6669109.

[13] C. Affleck, A. Jircitano, Passive gravity gradiometer navigation system, in: IEEE Symposium on Position Location and Navigation. A Decade of Excellence in the Navigation Sciences, IEEE, Las Vegas, NV, USA, 1990, pp. 60–66. doi:10.1109/PLANS.1990.66158.

[14] N. Laoué, A. Lepers, L. Deletraz. C. Faure, Neural Network Calibration of Airborne Magnetometers, in: 2023 IEEE 10th International Workshop on Metrology for AeroSpace (MetroAeroSpace), 2023. doi:10.1109/MetroAeroSpace57412.2023.10189964.

[15] Q. Han, Z. Dou, X. Tong, X. Peng, H. Guo, A Modified Tolles–Lawson Model Robust to the Errors of the Three-Axis Strapdown Magnetometer, IEEE Geoscience and Remote Sensing Letters, 14 2017, 334–338. doi:10.1109/LGRS.2016.2640188.

[16] I. Vallivaara, J. Haverinen, A. Kemppainen, Magnetic field-based SLAM method for solving the localization problem in mobile robot floor-cleaning task, in: 2011 15th International Conference on Advanced Robotics (ICAR), IEEE, Tallinn, Estonia, 2011, pp. 198–203. doi:10.1109/ICAR.2011.6088632.

[17] B. Li, T. Gallagher, A. G. Dempster, C. Rizos, How feasible is the use of magnetic field alone for indoor positioning?, in: 2012 International Conference on Indoor Positioning and Indoor Navigation (IPIN), IEEE, Sydney, Australia, 2012, pp. 1–9. doi:10.1109/IPIN.2012.6418880.

[18] G. Ouyang, K. Abed-Meraim, A survey of magnetic-field-based indoor localization, Electronics 11 (6) (2022) 864. doi:10.3390/electronics11060864.

[19] J. Aulinas, Y. R. Pétillot, J. Salvi, X. Lladó, The SLAM problem: a survey, in: Artificial Intelligence Research and Development, Frontiers in Artificial Intelligence and Applications, 2008, pp. 363–371. doi:10.3233/978-1-58603-925-7-363.

[20] I. Vallivaara, J. Haverinen, A. Kemppainen, J. Röning, Simultaneous localization and mapping using ambient magnetic field, in: 2010 IEEE Conference on Multisensor Fusion and Integration, IEEE, Salt Lake City, USA, 2010, pp. 14–19. doi:10.1109/MFI.2010.5604465.

[21] X. Wang, C. Zhang, F. Liu, Y. Dong, X. Xu, Exponentially weighted particle filter for simultaneous localization and mapping based on magnetic field measurements, IEEE Transactions on Instrumentation and Measurement 66 (7) (2017) 1658–1667. doi:10.1109/TIM.2017.2664538.

[22] F. Viset, R. Helmons, M. Kok, An Extended Kalman Filter for Magnetic Field SLAM Using Gaussian Process Regression, Sensors 22 (2022) 2833. doi:10.3390/s22082833.

[23] M. Zmitri, H. Fourati, C. Prieur, Magnetic Field Gradient-Based EKF for Velocity Estimation in Indoor Navigation, Sensors 20 (2020) 5726. doi:10.3390/s20205726.

[24] Y. H. Kim, H. J. Kim, J. H. Lee, S. H. Kang, E. J. Kim, J. W. Song, Sequential batch fusion magnetic anomaly navigation for a low-cost indoor mobile robot, Measurement 213 (2023) 112706. doi:10.1016/j.measurement.2023.112706.

[25] A. Canciani, J. Raquet, Absolute positioning using the Earth's magnetic anomaly field, NAVIGATION: Journal of the Institute of Navigation 63 (2) (2016) 111–126. doi:10.1002/navi.138.

[26] A. Canciani, J. Raquet, Airborne magnetic anomaly navigation, IEEE Transactions on Aerospace and Electronic Systems 53 (1) (2017) 67–80. doi:10.1109/TAES.2017.2649238.

[27] T. N. Lee, A. J. Canciani, MagSLAM: Aerial simultaneous localization and mapping using Earth's magnetic anomaly field, Navigation 67 (1) (2020) 95–107. doi:10.1002/navi.352.

[28] A. Gnadt, Machine Learning-Enhanced Magnetic Calibration for Airborne Magnetic Anomaly Navigation, AIAA SCITECH 2022 Forum, doi.org/10.2514/6.2022-1760.

[29] Ł Jankowski, D. Pisarski, R. Konowrocki, B. Popławski, R. Faraj, Efficient real-time positioning using Bayesian analysis and magnetic anomaly field, Measurement 233 (2024) 114738 doi:10.1016/j.measurement.2024.114738.

[30] J. Elfring, E. Torta, R. van de Molengraft, Particle Filters: A Hands-On Tutorial, Sensors 21(2) (2021) 438. doi:10.3390/s21020438.

[31] F. Gustafsson, F. Gunnarsson, N. Bergman, U. Forssell, J. Jansson, R. Karlsson, Particle filters for positioning, navigation, and tracking, IEEE Transactions on Signal Processing 50(2) (2002) 425-437. doi:10.1109/78.978396.

[32] E. Le Grand, S. Thrun, 3-Axis magnetic field mapping and fusion for indoor localization, in: 2012 IEEE International Conference on Multisensor Fusion and Integration for Intelligent Systems (MFI), IEEE, Hamburg, Germany, 2012, pp. 358–364. doi:10.1109/MFI.2012.6343024.

[33] P. Robertson, M. Frassl, M. Angermann, M. Doniec, B. J. Julian, M. G. Puyol, M. Khider, M. Lichtenstern, L. Bruno, Simultaneous localization and mapping for pedestrians using distortions of the local magnetic field intensity in large indoor environments, in: International Conference on Indoor Positioning and Indoor Navigation, IEEE, Montbeliard, France, 2001, pp. 1–10. doi:10.1109/IPIN.2013.6817910.

[34] A. Solin, M. Kok, N. Wahlström, T. B. Schon, S. Sarkka, Modeling and interpolation of the ambient magnetic field by Gaussian processes, IEEE Transactions on Robotics 34 (4) (2018) 1112–1127. doi:10.1109/TRO.2018.2830326.

[35] N. Wahlström, M. Kok, T. B. Schön, F. Gustafsson, Modeling magnetic fields using Gaussian processes, in: 2013 IEEE International Conference on Acoustics, Speech and Signal Processing, IEEE, Vancouver, Canada, 2013, pp. 3522–3526. doi:10.1109/ICASSP.2013.6638313.

[36] R. Garnett, Bayesian Optimization, Cambridge University Press, Cambridge, 2023.

[37] C. E. Rasmussen, C. K. I. Williams, Gaussian Processes for Machine Learning, The MIT Press, Cambridge, 2006.

[38] P. Alken, E. Thébault, C.D. Beggan et al, International Geomagnetic Reference Field: the thirteenth generation, Earth Planets Space 73 (49) (2021). doi:10.1186/s40623-020-01288-x.

[39] Magnetic Anomaly Map of Poland, Polish Geological Institute, 2003. https://www.pgi.gov.pl/images/stories/Geofizyka/OPolech/mapa%20magnetyczna%20polski%20(1%20mln).pdf

[40] A. Døssing, E. Lima Simoes da Silva, G. Martelet, T. Maack Rasmussen, E. Gloaguen, J. Thejll Petersen, J. Linde, A High-Speed, Light-Weight Scalar Magnetometer Bird for km Scale UAV Magnetic Surveying: On Sensor Choice, Bird Design, and Quality of Output Data, Remote Sensing 13 (4) (2021) 649. doi:10.3390/rs13040649.

[41] "Mavlink Guide." Accessed February 4, 2025. https://mavlink.io/.

[42] "Dronecan." Accessed February 4, 2025. https://dronecan.github.io/.

[43] "SITL Simulator (Software in the Loop)." ArduPilot. Accessed February 3, 2025. https://ardupilot.org/dev/docs/sitl-simulator-software-in-the-loop.html.

[44] "MAVProxy." ArduPilot. Accessed February 4, 2025. https://ardupilot.org/mavproxy.

[45] Office of the Federal Register, National Archives and Records Administration, 47 CFR § 73.208 - Reference points and distance computations, (2023):87-88, https://www.govinfo.gov/app/details/CFR-2023-title47-vol4/CFR-2023-title47-vol4-sec73-208.